

# Probing multiple populations of compact binaries with third-generation gravitational-wave detectors

KEN K. Y. NG,<sup>1,2</sup> SALVATORE VITALE,<sup>1,2</sup> WILL M. FARR,<sup>3,4</sup> AND CARL L. RODRIGUEZ<sup>5</sup>

<sup>1</sup>*LIGO Laboratory, Massachusetts Institute of Technology, Cambridge, Massachusetts 02139, USA*

<sup>2</sup>*Kavli Institute for Astrophysics and Space Research, Massachusetts Institute of Technology, Cambridge, Massachusetts 02139, USA*

<sup>3</sup>*Department of Physics and Astronomy, Stony Brook University, Stony Brook, New York, 11794, USA*

<sup>4</sup>*Center for Computational Astrophysics, Flatiron Institute, 162 Fifth Avenue, New York 10010, USA*

<sup>5</sup>*McWilliams Center for Cosmology, Department of Physics, Carnegie Mellon University, 5000 Forbes Ave, Pittsburgh, Pennsylvania 15213, USA*

(Dated: January 2, 2022)

## ABSTRACT

Third-generation (3G) gravitational-wave (GW) detectors will be able to observe binary-black-hole mergers (BBHs) up to redshift of  $\sim 30$ . This gives unprecedented access to the formation and evolution of BBHs throughout cosmic history. In this paper we consider three subpopulations of BBHs originating from the different evolutionary channels: isolated formation in galactic fields, dynamical formation in globular clusters and mergers of black holes formed from Population III (Pop III) stars at very high redshift. Using input from populations synthesis analyses, we create two months of simulated data of a network of 3G detectors made of two Cosmic Explorers and Einstein Telescope, consisting of  $\sim 16000$  field and cluster BBHs as well as  $\sim 400$  Pop III BBHs. First, we show how one can use non-parametric models to infer the existence and characteristic of a primary and secondary peak in the merger rate distribution. In particular, the location and the height of the secondary peak around  $z \approx 12$ , arising from the merger of Pop III remnants, can be constrained at  $\mathcal{O}(10\%)$  level (95% credible interval). Then we perform a modeled analysis, using phenomenological templates for the merger rates of the three subpopulations, and extract the branching ratios and the characteristic parameters of the merger rate densities of the individual formation channels. With this modeled method, the uncertainty on the measurement of the fraction of Pop III BBHs can be improved to  $\lesssim 10\%$ , while the ratio between field and cluster BBHs can be measured with an uncertainty of  $\sim 100\%$ .

## 1. INTRODUCTION

Advanced gravitational-wave (GW) detectors such as LIGO (Aasi et al. 2015), Virgo (Acernese et al. 2015) and Kagra (Aso et al. 2013) have dramatically increased our ability to study stellar mass black holes and the environments in which they form. The latest catalog released by the LIGO-Virgo-Kagra (LVK) collaboration includes 39 new GW detections, most of which are binary black holes (BBHs), bringing the total number of stellar mass black holes detected with GWs to over 100 (Abbott et al. 2019a, 2020a). These observations have already allowed for interesting astrophysical measurements (Abbott et al. 2019a,b, 2020a,b), such as hints for multiple formation channels (Farr et al. 2017; Zevin et al. 2017; Belczynski et al. 2020; Wong et al. 2020b; Zevin et al. 2020; Callister et al. 2020a; Antonini & Gieles 2020), hierarchical merg-

ers (Fishbach et al. 2017; Gerosa & Berti 2017; Doctor et al. 2019; Kimball et al. 2019, 2020b; Gerosa et al. 2020; Tiwari & Fairhurst 2020), as well as constraints on stellar physics (Farmer et al. 2020; Fragione & Loeb 2020; Bavera et al. 2020a), primordial BHs (Ali-Haïmoud et al. 2017; Bird et al. 2016; Sasaki et al. 2016; Wong et al. 2020a; Hall et al. 2020; Boehm et al. 2020; Hütsi et al. 2020) and ultralight bosons (Arvanitaki et al. 2017; Brito et al. 2017; Ng et al. 2019, 2020). Therefore, the growing set of BBHs enable studying both the properties of individual sources, as well as those of the underlying populations.

One of the key questions that can be addressed by GW astrophysics is how many such populations exist, and what are their characteristics. Multiple approaches have been proposed to address these questions, which ultimately rely on looking for features that would be expected in the BBH generated by each channel, such as their mass and spin distribution (Vitale et al. 2017;

Stevenson et al. 2015; Farr et al. 2018, 2017; Fishbach & Holz 2017; Fishbach et al. 2020; Kimball et al. 2020a; Talbot & Thrane 2017, 2018; Doctor et al. 2019; Bouffanais et al. 2019; Miller et al. 2020; Safarzadeh et al. 2020; Fishbach & Holz 2020), eccentricity distribution (Lower et al. 2018) or redshift distribution (Fishbach et al. 2018; Callister et al. 2020b). However, due to the limited sensitivity of current GW detectors, the observed BBHs are relatively “local”, with redshift  $z \lesssim 1$  (Abbott et al. 2019a,b, 2020a,b; Roulet et al. 2020; Venumadhav et al. 2020). Even as LIGO, Virgo and Kagra improve their sensitivities with the implementation of frequency dependent quantum squeezing (McCuller et al. 2020), and better low-frequency isolation (Yu et al. 2018), the detectors horizon will reach  $z \sim 3$  only for the heaviest systems (Abbott et al. 2016; Hall & Evans 2019).

Second-generation detectors will therefore be unable to access mergers at redshifts larger than a few. This likely precludes the possibility of detecting binaries whose component black holes originated directly from the Population III (Pop III) stars, whose formation peak could be as high as  $z \sim 10$ . Primordial black holes (Kinugawa et al. 2014, 2016; Belczynski et al. 2017; Hartwig et al. 2016; Raidal et al. 2017, 2019), might also be out of reach for existing facilities<sup>1</sup>. This will not be the case in the era of third-generation (3G) GW detectors such as Cosmic Explorer (CE) (Abbott et al. 2017; Reitze et al. 2019) and Einstein Telescope (ET) (Van Den Broeck 2010; Punturo et al. 2010; Maggiore et al. 2020). In fact, 3G detectors will have horizons up to  $z \gtrsim 30$  and enable accessing most of the BBHs throughout the cosmic history (Hall & Evans 2019). Therefore, both detections and not-detections of high redshift BBHs with 3G detectors can provide significant constraints on the properties of Pop III remnants. This is particularly important as the remnants of Pop III stars might be the light seeds that led the formation of supermassive black holes early in cosmic history (Greene et al. 2020). Whereas the space-based gravitational-wave detector LISA (Amaro-Seoane et al. 2017) and electromagnetic missions such as the X-ray observatory Lynx (Gaskin et al. 2019) might reveal the presence of heavy (i.e.  $M \gtrsim 100 M_{\odot}$ ) black holes at redshifts of 10, ground-based 3G detectors might very well be the only way to searching for smaller building blocks: stellar mass black holes.

Using the current *local* BBH merger rate estimate,  $\sim 25 \text{ Gpc}^{-3} \text{ yr}^{-1}$  (Abbott et al. 2020b), the total merger

rate of the BBHs in the Universe is  $\sim 10000$  per month, if the merger rate density follows the same evolution as the star formation rate (SFR) (Regimbau et al. 2017). Nearly all of these BBHs would be detectable by 3G detectors, and most of which will also have very high signal-to-noise ratio (SNR), leading to very precise distance (and hence redshift, assuming a known cosmology) measurements (Vitale 2016; Vitale & Evans 2017; Vitale & Whittle 2018). The large number of loud observations thus allows inferring the morphology of merger rate densities, in both parametric and non-parametric ways (Van Den Broeck 2014; Vitale et al. 2019; Safarzadeh et al. 2019; Romero-Shaw et al. 2020). In Vitale et al. (2019), we showed how combining redshift measurements of tens of thousands of GW observations in 3G detectors and assuming all BBHs are formed in galactic fields, one can infer the SFR history and the time-delay distribution. In light of the properties of the BBHs detected by LIGO and Virgo in the last few years, it has become harder to assume that all black holes are formed in galactic fields, since many of the black holes being detected are consistent with having formed dynamically, in globular or nuclear clusters or in the disks of active galactic nuclei (AGN) (Bartos et al. 2017; Yi & Cheng 2019; Yang et al. 2019, 2020; Gröbner et al. 2020; Tagawa et al. 2020b,c,a; Samsing et al. 2020). In this paper, we greatly extend or previous work (Vitale et al. 2019) and explore the possibility of simultaneously identifying and constraining the properties of *multiple* formation channels. In particular, we simulate universes where black holes can be formed in galactic fields, globular clusters and from Pop III stars. We show how well one can constrain the properties of each channel, and their branching ratios. In particular, we focus on the evidence for a high-redshift ( $z \gtrsim 5$ ) population, which would be the smoking gun of formation outside of the traditional evolutionary pathways. The rest of this paper is structured as follows: we first introduce the astrophysical formation channels in Sec. 2, then briefly review the Bayesian statistical methods used for the analysis in Sec. 3 and the simulation setup in Sec. 4. After going through the results in Sec. 5, we discuss their possible implications in Sec. 6.

## 2. ASTROPHYSICAL MODELS

In this section we summarize the main astrophysical properties of the BBH formation channels that we consider in the paper. Astrophysical BBHs are believed to form in various environments, such as binary stellar evolution in galactic fields (O’Shaughnessy et al. 2017; Dominik et al. 2012, 2013, 2015; de Mink & Belczynski 2015; Belczynski et al. 2016; Stevenson et al. 2017; Mapelli et al. 2019; Breivik et al. 2020; Bavera et al.

<sup>1</sup> We note that there are studies suggesting the heaviest BBH detected in the first part of LIGO/Virgo O3 run - GW190521 (Abbott et al. 2020c,d) - may be a Pop III BBH (Kinugawa et al. 2020; Tanikawa et al. 2020).

2020b; Broekgaarden et al. 2019), dynamical formation through multi-body interactions in star clusters (from low-mass stars to large nuclear star clusters) (Portegies Zwart & McMillan 2000; Antonini & Gieles 2020; Santoliquido et al. 2020; Rodriguez et al. 2015, 2016; Rodriguez & Loeb 2018; Di Carlo et al. 2019; Kremer et al. 2020; Rodriguez et al. 2015, 2016; Rodriguez & Loeb 2018; Antonini & Gieles 2020) or AGN disk (Bartos et al. 2017; Yi & Cheng 2019; Yang et al. 2019, 2020; Gröbner et al. 2020; Tagawa et al. 2020b,c,a; Samsing et al. 2020), from Population III (Pop III) stars (Kinugawa et al. 2014, 2016; Hartwig et al. 2016; Belczynski et al. 2017) or primordial black holes (Carr & Hawking 1974; Ali-Haïmoud et al. 2017; Clesse & García-Bellido 2017; Bird et al. 2016; Sasaki et al. 2016; Raidal et al. 2017, 2019; Wong et al. 2020a; Boehm et al. 2020; Hall et al. 2020).

For simplicity, in this paper we use galactic fields and globular cluster as the only main populations at low redshift, and Pop III stars as the only high-redshift channel. The analysis can be easily extended to even more population, at the price of an increased computational cost.

Hereafter, we label the BBHs in the three formation channels as *field binaries*, *cluster binaries* and *Pop III binaries*. Since an astrophysical BH is a remnant of stellar collapse, the merger rate history of each channel is correlated with the SFR and with the time delay from the binary formation to merger. Cluster and field binaries consist of BH-remnants leftover from Pop I/II stars, whose corresponding SFR peaks at late times:  $z \sim 3$  (Vangioni et al. 2015; Madau & Dickinson 2014). Accounting for the typical time delay between binary formation and merger ( $\sim 10$  Myr to  $\sim 10$  Gyr), their merger rates are expected to peak at around  $z \sim 2$  (Dominik et al. 2013; Belczynski et al. 2016; Mapelli et al. 2019; Rodriguez & Loeb 2018).

Pop III stars are instead formed at early times,  $z \gtrsim 10$ , from primordial gas clouds at extremely low metallicity (Vangioni et al. 2015; de Souza et al. 2011). The “metal-free” environment reduces the stellar wind mass loss during the binary evolution (Baraffe et al. 2001) so that Pop III stars might be more massive than the most recent stellar populations. Eventually, heavy BH remnants are left behind that merge in a short timescale, resulting on a merger rate density that could peak at around  $z \sim 10$  (Belczynski et al. 2016; Hartwig et al. 2016; Kinugawa et al. 2014, 2016).

The fact that different formation channels result in different merger rate distributions as a function of redshift, especially for Pop III remnants, can be exploited to infer properties of BBH populations solely based on

the redshift distribution of the detected sources. More elaborate tests can be envisaged, that also rely on other distinguishing features, e.g. masses, spins or eccentricity of the sources. In this study we will show that tests based on the redshift distribution alone can already provide significant constraints, while also having the benefit of being model-independent, at least in some of the implementations we demonstrate below. This seems particularly desirable, since the true distribution of intrinsic parameters such as masses and spins is highly uncertain, especially for Pop III remnants.

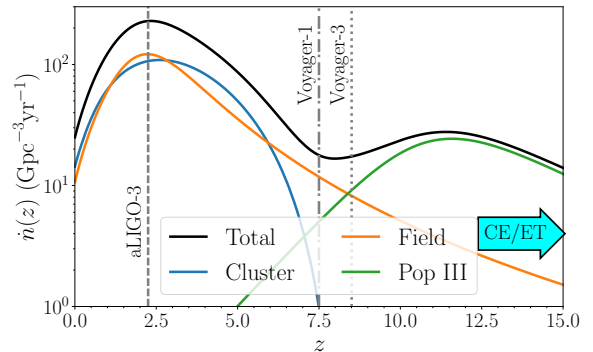


**Figure 1.** The merger rate densities of field (orange), cluster (blue) and Pop III (green) binaries, together with the overall merger rate (black), given by the sum of the three populations. For the purposes of this plot, field and cluster merger rate densities are normalized such that they produce the same number of binaries up to  $z$  of 15. The Pop III merger rate density is scaled so that its peak has an amplitude of 1/10 relative to the peak of the field and cluster merger rate densities. The vertical lines indicate the detector horizons,  $z_h$ , to BBHs with total masses (in the comoving frame)  $\leq 100M_\odot$ , in a network of three advanced detectors ( $z_h \sim 2.25$ ), a single Voyager (Adhikari et al. 2019) ( $z_h \sim 8.5$ ) and a network of three Voyager-like detectors ( $z_h \sim 12.1$ ), respectively (Hall & Evans 2019). The SNR threshold for detection is set to be 8 for a single detector and 12 for a detector network.

In Fig. 1 we show the “true” merger rate densities of three formation channels we use in this study, and focus on key features of their shapes (we will discuss later the branching ratios, i.e. the relative scale). The rate densities of field (orange), cluster (blue) and Pop III (green) binaries are phenomenological fits (details in Appendix B, Eqs. (B7), (B8) and (B9)) of the population synthesis simulation from Belczynski et al. (2016); Rodriguez & Loeb (2018); Belczynski et al. (2017), respectively. We notice that the high-redshift tail of the cluster merger rate density is much steeper than that of the field binaries. This is largely due to the choice of model: the cluster merger rates are based on the model of globular cluster formation from (El-Badry et al. 2019), which goes to zero at  $z \sim 10$ . That, combined with the delay between

cluster formation and BBH mergers (since BHs in clusters can only merge after the cluster has formed *and* the BHs have sunk to the center due to dynamical friction, a process which can take  $\sim 100\text{Myr}$  (e.g., Morscher et al. 2015)) causes a steeper slope in the merger rate at high  $z$ . The field and cluster merger rate densities peak at similar values,  $z \sim 2.2$  and  $z \sim 2.6$ , respectively, whereas the Pop III merger rate density peaks much later, at  $z \sim 11.6$ .

The vertical lines in Fig. 1 report the horizon of future ground-based detector networks. Advanced detector networks can observe BBHs up to the low-redshift peak of the merger rate densities of the two dominating channels, field and clusters. However, as the plot shows, for  $z \lesssim 2$ , the merger rate densities of both field and cluster binaries are quite similar. Hence advanced detectors are unlikely to be able to disentangle the two channels using only redshift information (as mentioned above, one can use other features, at the price of making the analysis more model-dependent). The situation improves with a single Voyager detector (“Voyager-1” line), which can access most of the field and cluster binaries up to  $z \lesssim 8$  and therefore exploit the expected difference in their merger rate after the peak to characterize the two channels. A network of 3 Voyager-like detectors (“Voyager-3” line) can extend the horizon to a redshift where the contribution to the total merger rate of the field and the Pop III channel might become comparable. However, it is only with 3G detectors that one can access the peak of the merger rate from Pop III. In fact, the horizon of CE and ET to heavy BBHs is outside of the range of Fig. 1 (as indicated by the cyan arrow in the bottom right corner), at  $z \sim 100$ . As we will show in the following sections the fact that the horizon of 3G detectors extends well beyond the expected peak of Pop III mergers allows for both modeled and unmodeled tests of the existence of such subpopulation.

### 3. STATISTICAL MODELS

Here, we briefly review the main statistical tool used in the analysis, i.e. the hierarchical Bayesian inference framework (Farr et al. 2015; Mandel et al. 2019; Thrane & Talbot 2019; Wysocki et al. 2019; Vitale 2020). We model the production mechanism of BBHs as an inhomogeneous Poisson process whose differential merger rate in the detector frame <sup>2</sup> is given by

$$\frac{dR^d}{dz}(z | \mathbf{\Lambda}, R^d) = \frac{1}{1+z} \frac{dR}{dz}(z | \mathbf{\Lambda}, R), \quad (1)$$

<sup>2</sup>  $R$  and  $R^d$  measure mergers per unit time. The clocks used to measure the time interval, the detector’s or the ones comoving with the sources, determine the frame in which the rate is calculated.

where  $dR/dz$  is the differential merger rate in the comoving frame characterized by the “shape parameters”  $\mathbf{\Lambda}$  and an overall normalization factor given by the total merger rate in the comoving frame  $R = \int \frac{dR}{dz} dz$ . The factor  $1/(1+z)$  accounts for the cosmological time dilation effect so that the total merger rate in the detector frame is

$$R^d = \int \frac{dR^d}{dz} dz = \int \frac{1}{1+z} \frac{dR}{dz} dz. \quad (2)$$

The vector of shape parameters  $\mathbf{\Lambda}$  contains the quantities which are used to model the underlying physical populations (see Sec. 4).

One can write the hyper-posterior of the population parameters  $\mathbf{\Lambda}$  and  $R^d$  given a set of  $N_{\text{obs}}$  observations  $\mathbf{d} \equiv \{d_i\}_{i=1}^{N_{\text{obs}}}$  as:

$$\begin{aligned} & p(\mathbf{\Lambda}, R^d | \mathbf{d}) \\ & \propto \left[ \prod_{i=1}^{N_{\text{obs}}} T^d \int dz_i p(d_i | z_i) \frac{dR^d}{dz}(z_i | \mathbf{\Lambda}, R^d) \right] e^{-R^d T^d} \pi(\mathbf{\Lambda}, R^d) \\ & \simeq \left[ \prod_{i=1}^{N_{\text{obs}}} T^d \frac{1}{M_i} \sum_{j=1}^{M_i} \frac{dR^d}{dz}(z_{ij} | \mathbf{\Lambda}, R^d) \right] e^{-R^d T^d} \pi(\mathbf{\Lambda}, R^d). \end{aligned} \quad (3)$$

In going from the second to the last line of Eq. (3), we have approximated the integrals with discrete sums. For the  $i$ -th source, this amounts to calculating an average of the merger rate evaluated at the  $M_i$  points  $\{z_{ij}\}_{j=1}^{M_i}$  drawn from the likelihood  $p(d_i | z_i)$  of the  $i$ -th source. In the third line,  $\pi(\mathbf{\Lambda}, R^d)$  is the hyper-prior, and  $T^d$  is the experiment duration in the detector frame.

In the study, we follow two approaches to construct  $dR/dz$ : (i) a “nonparametric” approach that utilizes Gaussian process regression (GPR) to infer  $dR/dz$  as a piecewise function over several redshift bins (Mandel et al. 2017); and (ii) a “parametric” approach in which we assume phenomenological functions to model various subpopulations (Farr et al. 2015; Vitale et al. 2019).

We will find more useful to quote the *volumetric* merger rate density, defined for the  $k$ -th subpopulation as

$$\dot{n}_k(z) \equiv dR_k/dV_c,$$

where  $dV_c/dz$  is the differential comoving volume. Then, the merger rate history  $dR_k^d/dz$  in the detector frame as a function of redshift for the  $k$ -th subpopulation is:

$$\frac{dR_k^d}{dz}(z | \mathbf{\Lambda}_k, R_k^d) = \frac{1}{1+z} \frac{dV_c}{dz} \dot{n}_k(z | \mathbf{\Lambda}_k, R_k), \quad (4)$$

where the subscript  $k$  denotes the relevant quantities of the  $k$ -th subpopulation.

The overall merger rate can be expressed as the sum of the individual merger rates of all  $P$  subpopulations ( $P = 3$  in our analysis), i.e.

$$\frac{dR^d}{dz}(z | \mathbf{\Lambda}, \mathbf{R}^d) = \sum_k^P \frac{dR_k^d}{dz}(z | \mathbf{\Lambda}_k, R_k^d), \quad (5)$$

where the vectors  $\mathbf{\Lambda}$  and  $\mathbf{R}^d$  contains all  $\mathbf{\Lambda}_k$ 's and  $R_k^d$ 's, respectively. Since  $\sum_k^P R_k = R$  and  $\sum_k^P R_k^d = R^d$ , we may rewrite Eq. (5) in terms of the branching ratios in the detector frame, i.e. the fraction of sources in each subpopulation,  $f_k \equiv R_k^d/R^d$ ,

$$\frac{dR^d}{dz}(z | \mathbf{\Lambda}, R^d) = R^d \sum_k^P f_k p_k^d(z | \mathbf{\Lambda}_k), \quad (6)$$

where  $p_k^d(z | \mathbf{\Lambda}_k)$  is the normalized merger rate of the  $k$ -th population in the detector frame, and the  $f_k$ 's are subject to the constraint  $\sum_k^P f_k = 1$ . Since we expect the fraction of Pop III binaries to be small, it is more convenient to introduce the fraction of cluster binaries over the sum of field and cluster binaries,  $\hat{f}_G \equiv f_G/(f_G + f_F)$ .

Therefore, for the parametrized analysis we model the merger rates of the three subpopulations in terms of several phenomenological parameters, which are treated as unknowns, together with the branching ratios (Sec. 4). The total merger rate in Eq. 3 is thus calculated by adding up the contribution of each channel. On the other hand, in the unmodeled approach, we measure the overall  $\frac{dR}{dz}(z | \mathbf{\Lambda}, R)$  directly, without making any assumption about the individual subpopulations that might be contributing to it.

More details on the two approaches can be found in Appendices A and B, whereas the hyper-priors are described in the Appendix C. Throughout the study, we assume Planck 15 cosmology (Ade et al. 2016).

#### 4. SIMULATION DETAILS

In this section we describe how we prepare the simulated universes that will be analyzed with the methods described in the previous section.

First, we need to choose reference (i.e. “true”) merger rate densities that will be used to generate the redshift of the BBHs. We do so by means of the phenomenological curves in Eqs. (B7), (B8) and (B9). As described in Appendix B, these curves describe the morphology of each volumetric merger rate density, and are parametrized by, e.g., the rising slope at low redshift, the declining slope at high redshift, and the redshift at which the merger rate peaks. The phenomenological curves are obtained by fitting Eqs. (B7), (B8) and (B9) to the simulation results available in the literature (Belczynski et al. 2016;

Rodriguez & Loeb 2018; Belczynski et al. 2017). Specifically, we take the model-averaged simulation results of Refs. (Belczynski et al. 2016) and (Rodriguez & Loeb 2018) for field and cluster binaries, respectively, as well as “FS1” model’s result of (Belczynski et al. 2017) for Pop III binaries. We stress that our phenomenological fits include the effect of the time delay from binary formation to merger, as well as the impact of stellar metallicity on the binary evolution specified in the population synthesis analyses. In particular, this implies a quite remarkable fact: the same Madau-Dickinson function can be used both to fit the star formation rate (this is its normal use) and the merger rate density it implies, for different values of its parameters.

We use the following numbers as the “true” values of each curve parameters, when preparing our sources:

$$\begin{aligned} (\hat{\alpha}_F, \hat{\beta}_F, \hat{C}_F) &= (2.57, 5.83, 3.36), \\ (\hat{\mu}_G, \hat{\sigma}_G, \hat{t}_G) &= (1.63, 0.96, 0.66 \text{ Gyr}), \\ (\hat{a}_{\text{III}}, \hat{b}_{\text{III}}, \hat{z}_{\text{III}}) &= (0.66, 0.3, 11.6). \end{aligned}$$

While this fixes the true shape of the merger rate for each subpopulation, we still need to fix the amplitudes. We use 9 different values of relative the merger rate between cluster and field binaries,  $\hat{f}_G$ , equally spaced in the range from 0 to 1. For each value of  $\hat{f}_G$ , we consider two universes: one with and one without Pop III binaries.

Following the latest GWTC-2 result, we fix the local volumetric merger rate density to  $\dot{n}(0) = 25 \text{ Gpc}^{-3} \text{ yr}^{-1}$  (Abbott et al. 2020b). This yields  $R_F^d + R_G^d \approx 8000$  per month. In the universes with Pop III binaries, the Pop III fraction  $f_{\text{III}} \approx 0.024$  is chosen to generate an additional 200 sources per month coming from the Pop III channel. This number is chosen such that the peak merger rate density of Pop III binaries is  $\sim 10$  times smaller than the peak of the dominating channels. The nominal value of this peak,  $\dot{n}_{\text{III}}(z_{\text{III}}) \approx 20 \text{ Gpc}^{-3} \text{ yr}^{-1}$ , is consistent with the comparison of “FS1” model to the Pop I/II field binaries in Belczynski et al. (2016). We stress that the current predictions for the Pop III merger rate span a few orders of magnitudes, in either direction, relative to the one we are using (Belczynski et al. 2016; Hartwig et al. 2016; Kinugawa et al. 2014, 2016). This is because the formation efficiency of Pop III binaries greatly depends on the initial mass function of the Pop III stars and the distribution of the initial orbital separation (see Belczynski et al. (2016); Hartwig et al. (2016)). Since  $\dot{n}_{\text{III}}$  declines rapidly at later cosmic time, it does not significantly contributes to  $\dot{n}(0)$ .

To ensure a reasonable measurement of luminosity distance, which typically requires three or more detectors,

we choose a baseline detector network with one CE in Australia, one CE in the United States, and one ET in Europe (Vitale 2016; Vitale & Evans 2017; Vitale & Whittle 2018). Generally speaking, not all BBHs within the detector horizon can be detected with SNRs over some thresholds, depending on their orientation and intrinsic parameters. This results in a Malmquist bias (Mandel et al. 2019; Vitale 2020). However, the efficiency only drops to 50% at  $z \sim 20$  for a typical  $30M_{\odot} - 30M_{\odot}$  BBH. Therefore, we limit our analysis to the redshift range  $0 \leq z \leq 15$  and neglect selection effect.

Finally, we simulate a month of data in the following way. We first draw the set of true redshifts,  $\{z_{\text{true}}\}$ , from the “true”  $dR/dz$  in each universe. Then, for each  $z_{\text{true},i}$ , we obtain the *observed* redshift,  $z_{\text{obs},i}$ , by drawing a random variable from a mock-up single-event likelihood conditional on  $z_{\text{true},i}$ . Following (Vitale et al. 2019), we approximate the likelihood for redshift as a lognormal distribution conditional on  $z_{\text{true},i}$  with a standard deviation  $\sigma_{\text{LN},i} = 0.017z_{\text{true},i}$ . Finally, we draw 100 single-event likelihood samples conditional on  $z_{\text{obs},i}$  with the same  $\sigma_{\text{LN},i}$  calculated previously. The second step is necessary in order to generate a scattering to the true value within the probable range of the single-event likelihood function. Otherwise, the alignment of the true value and the mean of the likelihood introduces systematic bias in the analysis.

To summarize, we generate 18 simulated universes. In all universes, we generate 16000 (two-months worth data) BBHs from field and cluster binaries with a given branching ratio  $\tilde{f}_{\text{G}}$ , and add 400 more Pop III observations for the 9 universes containing Pop III binaries.

## 5. RESULTS

With the simulations set up in each of the 18 universe as described in the previous section, we now report on the measurement of the total merger rate density (and of each individual population, for the phenomenological mixture model). As mentioned above, we will quote the *volumetric* merger rate density,  $\dot{n}(z) \equiv dR/dV_c$  rather than  $R$  itself.

### 5.1. Gaussian Process Regression

Figure 2 shows our inference on the volumetric merger rate  $\dot{n}$  obtained with the unmodeled GPR approach. The black colored bands report the 68% and 95% credible intervals for the universes without (left panel) and with (right panel) Pop III binaries. The colored lines show the true volumetric merger rate of the individual populations. For both of the panels the branching ratio between field and cluster binaries is  $\tilde{f}_{\text{G}} = 0.5$ . We find that the true  $\dot{n}$ 's

(black dashed lines) lie within the 95% credible intervals in both cases. While the relative uncertainty on  $\dot{n}$  is at a percent level at  $z \lesssim 6$ , it increases to  $\mathcal{O}(100\%)$  at  $z \gtrsim 8$ . This is because (i) the SNR of each source decreases with the distance, and (ii) the number of sources in each redshift bin is decreasing as the differential comoving volume shrinks at earlier times in the history of the universe.

Perhaps the most attractive feature of the unmodeled analysis, is that we can find some evidence for the presence of an high-redshift subpopulation, even without strong modeling. The simplest way of doing this is to look for local peak(s) in  $\dot{n}$ . At the very minimum, we would expect to find evidence for the “main” peak at  $z \sim 2$ , arising from the merger in fields and clusters, while high-redshift peaks would be indicative of a different subpopulation.

We implement this peak finder algorithm simply by asking that the first derivative of  $\dot{n}$  is zero and the second is negative:  $d\dot{n}/dz = 0$  and  $d^2\dot{n}/dz^2 < 0$ . Some care is required to avoid false positives due to natural oscillations in the results of the GRP which are not due to astrophysical maxima (or minima) but only to the underlying Gaussian process. These are particularly visible at high redshifts in Fig. 2(a). To mitigate the effect of these fluctuation and suppress the unphysical peaks, we require the height of any high redshift peaks to be at least 1/10 of the height of the low redshift peak, as well as an intra-peak separation larger than  $\Delta z = 1$ . These requirements are based on the expected excess of Pop III as discussed in Sec. 4 and arguably represent the only modeling involved in the GRP approach that we describe.

With these two restrictions, we count the number of peaks  $N_{\text{peak}}$  for each  $\dot{n}$  sample of the GRP in every simulated universe. The results are shown in Fig. 3 as a function of the true branching ratio cluster/field. For the universes without Pop III binaries, we recover a single peak, as expected, with  $> 99\%$  probability (purple histograms). This implies the non-existence of a secondary peak whose relative height is  $\geq 10\%$  of the primary peak. On the other hand, the true value for the number of peaks,  $N_{\text{peak}} = 2$ , is found at  $\gtrsim 90\%$  credibility for in the universes with Pop III binaries (yellow histograms).

We observe that in the universes with Pop III binaries the posterior on the number of peaks has a secondary mode at  $N_{\text{peak}} = 3$  for  $\tilde{f}_{\text{G}} \lesssim 0.5$ . We explain this as follows: for  $\tilde{f}_{\text{G}} \lesssim 0.5$ , the field binaries are the dominating channel, and as clear in Fig. 2 produce a flatter high-redshift tail than the cluster channel. Hence it is easier to produce multiple peaks due to fluctuation and induces a leakage to  $N_{\text{peak}} \geq 3$ . On the other hand, when

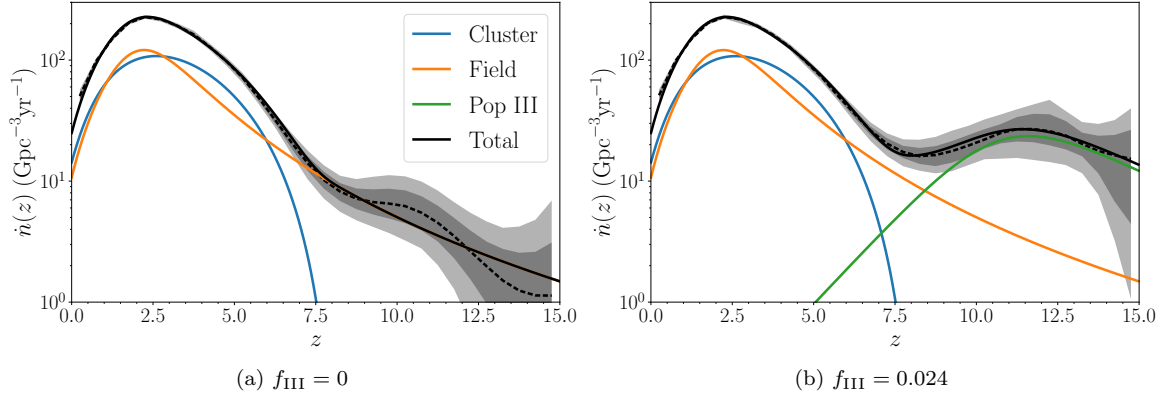


**Figure 2.** Reconstruction of  $\dot{n}$  for the  $\tilde{f}_G = 0.5$  universes without (left panel) and with (right panel) Pop III binaries using GPR. The grey color band and solid line shows the 68% (darker color) and 95% (lighter color) credible intervals, and the median of recovered  $\dot{n}$ , respectively. The black, orange and blue dashed lines are the fiducial  $\dot{n}$ ,  $\dot{n}_F$ , and  $\dot{n}_G$ , respectively. Since we cannot model each subpopulation with the nonparametric approach, no hyper-posterior can be drawn for each branch.

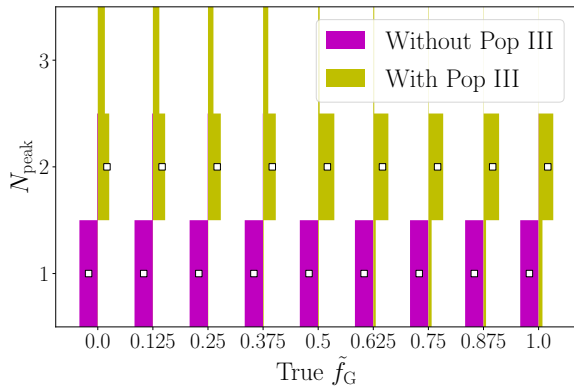


**Figure 3.** Posterior distributions of  $N_{\text{peak}}$  of  $\dot{n}$  for all 18 universes. Since  $N_{\text{peak}}$  is a discrete measure, the distributions are represented by histograms. For the universes without (purple) and without (yellow) Pop III binaries, the true  $N_{\text{peak}}$  are 1 and 2, respectively.

$\tilde{f}_G \gtrsim 0.5$ , the cluster binaries are dominating and do not contribute to the merger rate at  $z \gtrsim 8$  where Pop III population becomes the only source of BBHs, which makes the high-redshift peak narrower and hence easier to reveal. But the Poisson fluctuation of the high-redshift bins in  $dR/dz$  may still lead to an underestimation of the relative height below our 10% threshold, inducing a small contamination at  $N_{\text{peak}} = 1$ . We note that the above trend is subject to the model uncertainty of our chosen simulation data in the high-redshift region.

This method also allows measuring the location(s) of the peak(s), which would be useful to understand the population properties. For instance, the shift of the primary peak relative to the star formation rate could inform the typical time delay to merger and a hint of metallicity evolution (Chruslinska et al. 2019; Santoliquido et al. 2020). In addition, constraining the

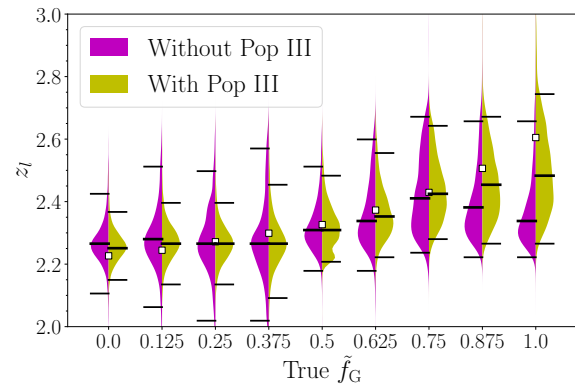


**Figure 4.** Hyper-posterior of  $z_l$  for all 18 universes. In each half-leaf, the upper and lower black dashes mark the 95% credible interval, and the middle black dash locates the median. The square markers indicate the true values of  $z_l$ .

high redshift peak to  $z \gtrsim 8$  would provide support to the existence of Pop III binaries.

We first show the inferred distribution of the low redshift peak,  $z_l$ , for all universes in Fig. 4. All measurements of  $z_l$  constrain the low redshift peaks to  $z < 3$ , with 95% credible-interval uncertainties of  $\sim 40\%$ . The true values are contained within the uncertainty.

Next, we look at the measurements of the high redshift peak's location  $z_h$  for the universes with Pop III binaries, as shown by the red violins in Fig. 5. In all cases, the true value  $\hat{z}_h = 11.6$  lies within the 95% credible intervals. The lower bound of the credible interval is above  $z \sim 7$  for all values of  $\tilde{f}_G$ , indicating that one can confidently place the secondary peak at redshift much larger than where the star formation peaks. The widths of the credible intervals decrease from  $\sim 50\%$  to  $\sim 25\%$  when  $\tilde{f}_G$  increases from 0 to 1. This may be again explained by

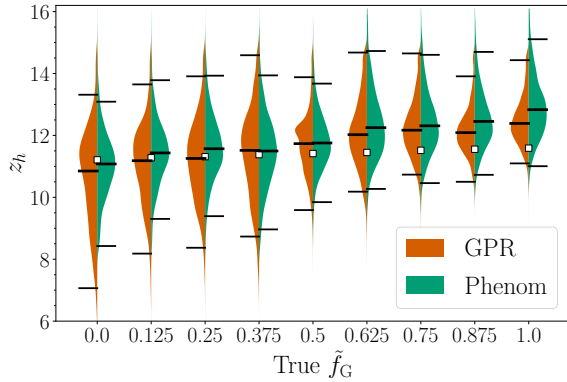


**Figure 5.** Hyper-posterior of  $z_h$  for the 9 universes with Pop III binaries, conditioned with  $\dot{n}(z_h) \geq 0.1\dot{n}(z_l)$  inferred by the GPR model (red) and the phenomenological (Phenom) model (green). Other plot settings are the same as Fig. 4.

the steeper redshift tail in the cluster population, which makes the Pop III peak easier to resolve.

### 5.2. Phenomenological recovery

Having shown how a simple non-parametric model can already provide insight into the existence of a high-redshift population of BBHs, we now repeat the hierarchical inference using the phenomenological model described in Sec. 3. The quantities that are measured, their meaning and the priors are fully described in Appendix B and C.

We start by showing the posteriors on the peak of the merger rate density for the Pop III BBHs, this time obtained as one of the parameters on which their phenomenological model depends, in Fig. 5, green violins. Remembering that the orange violins in the same plot reports the measurement we obtained with the GPR approach, we find that the two methods yield very consistent results, with the widths of 95% credible intervals varying by  $\sim 10\%$  at most. The consistency between the two approaches highlights the promise of the nonparametric approach in revealing the existence and location of an high-redshift population. However, as we have emphasized, the phenomenological model directly describes the morphology of each subpopulation and thus allows extracting information about each individual population, which cannot be accessed by the nonparametric approach.

In Fig. 6 we show the inferred  $\dot{n}$  for the simulated  $\tilde{f}_G = 0.5$  universes without (left panel) and with (right panel) Pop III binaries<sup>3</sup>. For each population, the solid line represents the true merger rate, whereas the dashed

line and the colored bands represents the median, and the 68%/95% credible intervals.

The total  $\dot{n}$  (black colored band) can be well constrained within a few percent level up to  $z \sim 6$ . For  $f_{\text{III}} = 0$ , the relative uncertainty rises to  $\sim 100\%$  at  $z \gtrsim 10$ . Even at low redshift, the uncertainty of  $\dot{n}_F$  (orange color band) and  $\dot{n}_G$  (blue color band) is about 50%,  $\sim 10$  times larger than that of the total rate,  $\dot{n}$ . This is because the morphology of  $\dot{n}_F$  and  $\dot{n}_G$  is similar at  $z \lesssim 3$ , where most of the BBHs can be detected with a precise distance measurement. Conversely,  $\dot{n}_F$  and  $\dot{n}_G$  are easier to distinguish at  $z \gtrsim 5$  where, as discussed before,  $\dot{n}_G$  is declining more rapidly than  $\dot{n}_F$ , which instead has a long tail at  $z \gtrsim 8$ . Overall, the similarity in the morphology of the low-redshift volumetric merger rate of the two dominating channels induces degeneracies, hence boosts uncertainties, in the the individual merger rates,  $\dot{n}_F$  and  $\dot{n}_G$ .

Considering now the universe with  $f_{\text{III}} = 0.024$  (right panel), we find that rate of Pop III curve (green colored band) near its peak at  $z \sim 12$  can be measured with a relative uncertainty of  $\sim 50\%$ , while the uncertainty of other channels remains similar to the universe with  $f_{\text{III}} = 0$ .

We compare the phenomenological recovery of the total  $\dot{n}$  to the GPR recovery (Fig. 2) for the same universes, and find that the typical uncertainty of  $\dot{n}$  is smaller by a factor of  $\sim 2$ . This is not surprising, since the phenomenological approach uses models for the subpopulations, which inform the recovery of the overall merger rate. Naturally, the price to pay for the improved precision is to have made the results depend on the goodness of the models.

Next, we look at the hyper-posteriors, i.e. at the posteriors of the variables that parametrize the individual subpopulations, as well as the branching ratios. First, we show the hyper-posterior of the dominating channels' parameters for the universe with  $(\tilde{f}_G, f_{\text{III}}) = (0.5, 0)$  (the same of Fig. 6(a)) in Fig. 7. Most of the shape parameters are measured with  $\sim 100\%$  uncertainty, e.g.  $\tilde{f}_G = 0.59^{+0.28}_{-0.27}$ . We note that there are a few interesting correlated pairs, such as  $(t_G, \tilde{f}_G)$  and  $(t_G, \sigma_G)$ . Since  $t_G$  characterizes the starting time of the merging cluster binaries, an earlier  $t_G$  shifts the peak of cluster population towards higher redshift where the cosmological volume is smaller. Hence  $\tilde{f}_G$  needs to be larger to keep the same number of cluster binaries. On the other hand, a smaller  $t_G$  tends to shift cluster population towards lower redshift. Then a larger  $\sigma_G$  is necessary to maintain a wide merger rate peak.

Next, we look at the hyper-posterior of the Pop III merger rate parameters for the same universe, as shown

<sup>3</sup> These are the same two universes of Fig. 2

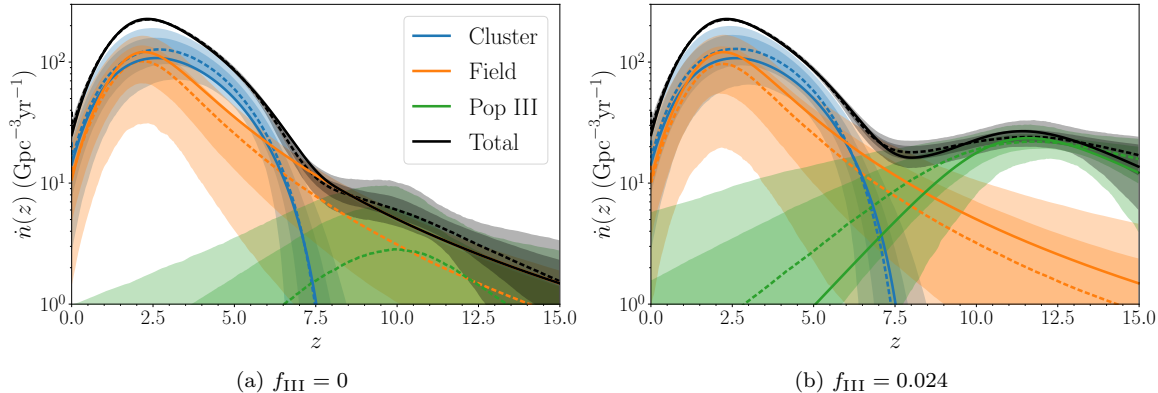


**Figure 6.** Reconstruction of merger rate densities for the  $\tilde{f}_G = 0.5$  universes without (left panel) and with (right panel) using phenomenological models. The orange, blue, green and black solid lines are the medians of the recovered  $\dot{n}_F$ ,  $\dot{n}_G$ ,  $\dot{n}_{\text{III}}$  and  $\dot{n}$ , respectively. The corresponding color bands are the 68% (darker colors) and 95% (lighter colors) credible intervals of the reconstruction. The true merger rate densities are shown as the dashed lines of the same colors. The green dashed line is invisible since there are no Pop III binaries in this universe.

by the purple contours in Fig. 8. We are able to constrain  $f_{\text{III}} \lesssim 0.02$ . Both  $a_{\text{III}}$  and  $b_{\text{III}}$  are very close to their priors, which make sense since  $f_{\text{III}}$  is small which implies no information about  $\dot{n}_{\text{III}}$  can be gained. On the other hand, the position of the peak,  $z_{\text{III}}$ , is shifted towards lower values relative to its prior to suppress the contribution from  $\dot{n}_{\text{III}}$  to the high-redshift total merger rate, which in this universe is entirely determined by the field binaries.

As a comparison, we now focus on the result for the universe with  $f_{\text{III}} = 0.024$  (this is the same as in Fig. 6(b)). In Fig. 8, the orange contours show the hyper-posterior of  $\dot{n}_{\text{III}}$ 's parameters. While the shape parameters of  $a_{\text{III}}$  and  $b_{\text{III}}$  are still not well constrained, the peak  $z_{\text{III}} = 11.75^{+1.92}_{-1.91}$  is measured with  $\sim 30\%$  relative uncertainty. Importantly,  $f_{\text{III}} = 0$ , i.e., the absence of a Pop III channel, is excluded from the 95% credible interval of the marginalized  $f_{\text{III}}$  posterior. This provides strong evidence of the existence of Pop III binaries in our simulated data.

It is worth looking at the correlations between the hyper-parameters of the various subpopulations. Some correlation should be expected since for example the number of sources at high redshift might be potentially explained by the model either with a larger fraction of field binaries, which have a fat high-redshift tail, or by binaries in the Pop III channel. In Fig. 9, we show the marginalized 2D contours of the  $(\tilde{f}_G, f_{\text{III}})$  pair for the universes  $\tilde{f}_G = 0.5$  without (purple) and with (yellow) Pop III. A positive correlation between the two parameters is clearly visible. This is caused by the partial model degeneracy between  $\dot{n}_F$  and  $\dot{n}_{\text{III}}$ . This goes exactly in the direction one would expect: underestimating  $f_{\text{III}}$  means that the model must increase the

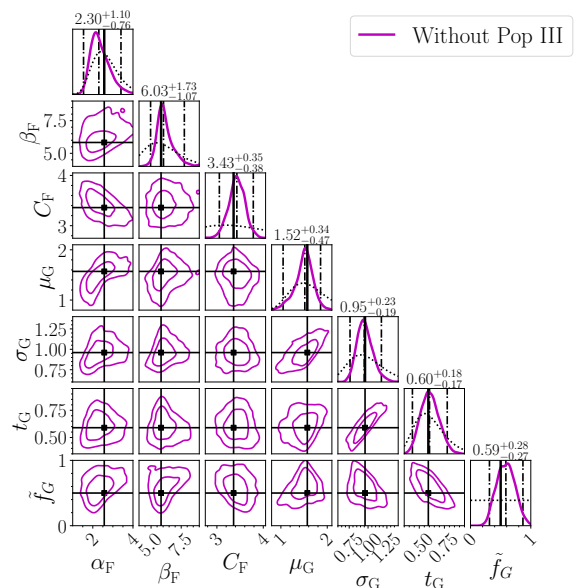


**Figure 7.** Hyper-posterior of the dominating channels' hyperparameters,  $(\alpha_F, \beta_F, C_F, \mu_G, \sigma_G, t_G, \tilde{f}_G)$ , for the universe with  $(\tilde{f}_G, f_{\text{III}}) = (0.5, 0)$  (the same of Fig. 6(a)). For each marginalized 1D posterior (purple solid line in each diagonal slot), the left and right black dashed-dotted lines mark the 95% highest posterior density credible interval, the middle black dashed-dotted line locates the median, and the black dotted line shows the prior. The numerical values of median values and 95% credible intervals are reported above the diagonal slots. The off-diagonal slots show the marginalized 2D posteriors, with the contours representing the 68% and 95% credible intervals. The black markers and solid lines indicate the true values, which lie within the 68% credible interval. The statistical behavior for the universe with Pop III is very similar.

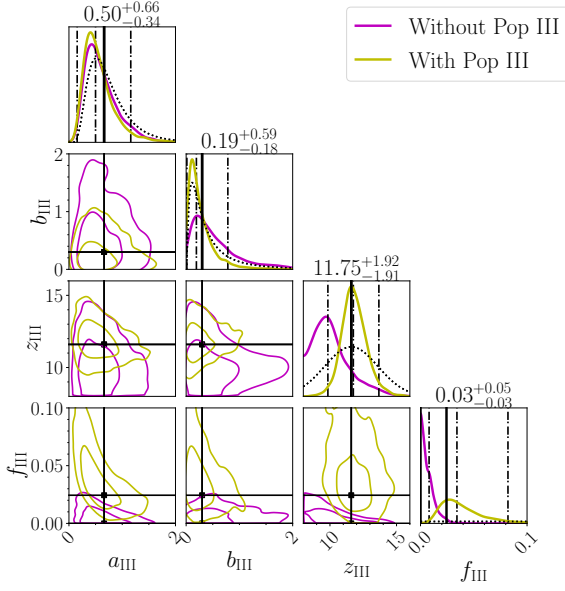


**Figure 8.** Hyper-posterior of the Pop III population's hyper-parameters,  $(a_{\text{III}}, b_{\text{III}}, z_{\text{III}}, f_{\text{III}})$ , for the universes  $(\tilde{f}_{\text{G}}, f_{\text{III}}) = (0.5, 0)$  (purple) and  $(\tilde{f}_{\text{G}}, f_{\text{III}}) = (0.5, 0.024)$  (yellow). The plot setting is the same as in Fig. 7. Only the medians and 95% credible intervals for the universe with Pop III binaries (orange) are indicated by the dashed-dotted lines and reported above the diagonal slots.

number of field binaries to account at least partially for the high-redshift binaries. But if the number of field binaries increases,  $\tilde{f}_{\text{G}}$  must decrease.

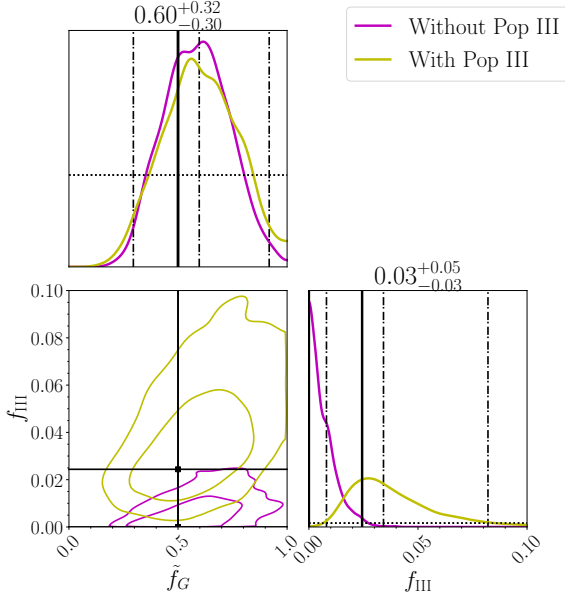


**Figure 9.** Hyper-posterior of the population fractions,  $(\tilde{f}_{\text{G}}, f_{\text{III}})$ , for the universe  $(\tilde{f}_{\text{G}}, f_{\text{III}}) = (0.5, 0.024)$ . The plot setting is the same as in Figs. 7 and 8.

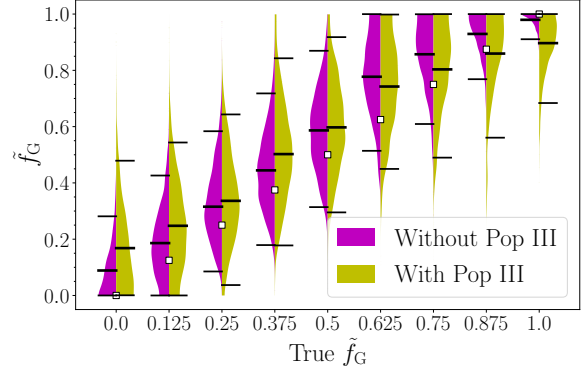


**Figure 10.** Marginalized hyper-posteriors of  $\tilde{f}_{\text{G}}$  for all 18 universes, split into two categories: without (purple) and with (yellow) Pop III binaries. The plot setting is the same as in Fig. 4.

The partial correlation between  $\dot{n}_{\text{F}}$  and  $\dot{n}_{\text{III}}$  manifests itself in two other interesting ways. First, we observe an increase in the uncertainty of  $\tilde{f}_{\text{G}}$  when Pop III mergers are present. In Fig. 10, we show violin plots for the marginalized  $\tilde{f}_{\text{G}}$  posteriors at different true  $\tilde{f}_{\text{G}}$  values. The purple and yellow violins correspond to the universes with and without Pop III binaries, respectively. While the true values lie inside the 95% credible interval in all cases, the uncertainties increase by  $\sim 10\%$  for the universes with Pop III binaries.

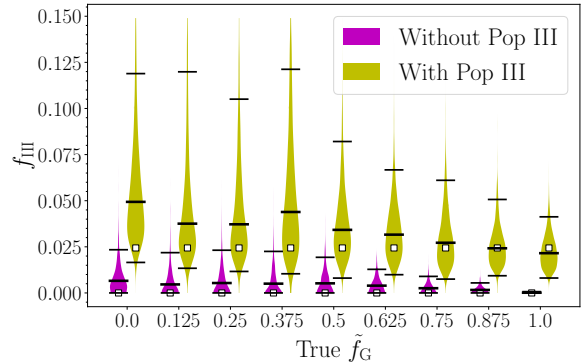


**Figure 11.** Marginalized hyper-posteriors of  $f_{\text{III}}$  for all 18 universes. The plot setting is the same as in Fig. 4.

Second, the uncertainty in  $f_{\text{III}}$  decreases as  $\tilde{f}_{\text{G}}$  increases. Figure 11 is a plot similar to Fig. 10, but showing the marginalized  $f_{\text{III}}$  posteriors in different universes. When Pop III binaries are present, the uncertainty stays roughly constant  $\Delta f_{\text{III}} \sim 0.1$  up to  $\tilde{f}_{\text{G}} \lesssim 0.5$ , after which it drops gradually to  $\Delta f_{\text{III}} \sim 0.05$  at  $\tilde{f}_{\text{G}} = 1$ . A similar trend is observed when no Pop III binaries exist: the uncertainty drops from  $\sim 2.5\%$  to  $\lesssim 0.1\%$ . This is because  $\dot{n}_{\text{F}}$  has a longer tail in the high redshift  $z \gtrsim 8$ , and

is easier to be confused with a small excess of Pop III population.

## 6. DISCUSSIONS AND CONCLUSIONS

In this paper, we have shown that observations made by a network of 3G detectors can be used to infer the properties of different BBH populations using redshift-only information. The larger horizon of a 3G detector network allows accessing thousands of BBHs per month up to  $z \sim 15$ , which is necessary to resolve the excess of high-redshift ( $z \gtrsim 8$ ) BBHs originated from Pop III stars. We consider  $\sim 16000$  binaries, roughly corresponding to two months of data, and multiple values of the branching ratio between binary formation in galactic fields and globular clusters. For every value of this branching ratio, we analyzed both a case where a few hundred Pop III BBHs are present, and one where they do not exist.

First, we consider a hierarchical inference approach based on a nonparametric reconstruction of the total volumetric merger rate density  $\dot{n}$ . We look for local peaks in the reconstructed total merger rate, and extract limited but useful information about the high-redshift population. By requiring that a possible high-redshift peak has an amplitude of at least 1/10 of the low-redshift peak, we find evidence for the presence of an high-redshift peak when Pop III binaries are included, and constrain its position to be in the range  $7 \leq z_h \leq 15$  for various mixing fractions between field and cluster binaries. Using the same approach, we rule out the existence of secondary-peak structure if there were no Pop III binaries. This minimally modeled measurement of the position of an high-redshift peak (or lack thereof) in the total binary merger rate might, with some model, be translated into measurement or an upper limit on the abundance of Pop III stars. With a similar approach, we are able to measure the position of a low-redshift peak, which might be used to investigate typical time delays between start formation and mergers.

Then, we considered a modeled analysis where a phenomenological model exist for each of the three subpopulations, which are characterized by a set of unknown hyper-parameters, measured from the data together with the (unknown) branching ratios. Among the most remarkable results, we found that irrespective of the true value of the relative abundances of field and cluster binaries, the Pop III fraction can be constrained to be  $f_{\text{III}} \gtrsim 0.01$  ( $f_{\text{III}} \lesssim 0.02$ ) at 95% credibility for the universes that have (do not have) Pop III binaries. In both cases, the branching ratio between field and cluster binaries can be measured with better than  $\sim 100\%$  uncertainty (95% credible interval). The precision on the measurement of the Pop III population mainly depends

on the morphology of the merger rate densities of the dominating channels in the high-redshift region. If the dominating channels predict a shallower declining slope at high redshift, an eventual contribution to the high-redshift merger rate from the Pop III population is less distinctive, introducing correlations with the dominating channels.

We emphasize that our analysis is only assuming two months worth of data. A back-of-the-envelope calculation assuming that the statistical uncertainty shrinks like  $1/\sqrt{N}$  would imply a factor of  $\sim 5$  improvement over the results we present here, after 5 years of data. In that scenario, the phenomenological approach could identify a fraction of Pop III mergers as small as  $f_{\text{III}} \sim 0.5\%$ . However, as stressed multiple times in this work, the phenomenological inference requires reliable models for the merger rate of the various formation channels, and will yield results which are as good as the models. On the other hand, the model independent approach, though intrinsically less precise, has the attractive feature of not requiring any specific modeling of the underlying subpopulation.

In this work, we have only considered three subpopulations: the galactic field and cluster binaries, as well as high-redshift Pop III binaries. As mentioned above, many other channels have been proposed and can plausibly contribute a sizeable fraction of the total rate. Our analysis can be trivially extended to include these and other subpopulations, at the price of increasing computational cost, correlations, and potentially degrading the measurement of some of the parameters. On the other hand, most of these different channels predict distinctive features in the BBHs they produce, beside their redshift distribution, for example masses, spins and eccentricity (Vitale et al. 2017; O’Shaughnessy et al. 2017; Dominik et al. 2012, 2013, 2015; de Mink & Belczynski 2015; Belczynski et al. 2016; Mapelli et al. 2019; Breivik et al. 2020; Stevenson et al. 2017; Antonini & Gieles 2020; Santoliquido et al. 2020; Rodriguez et al. 2015, 2016; Rodriguez & Loeb 2018; Di Carlo et al. 2019; Kremer et al. 2020; Bartos et al. 2017; Yi & Cheng 2019; Yang et al. 2019, 2020; Gröbner et al. 2020; Tagawa et al. 2020b,c,a; Samsing et al. 2020; Raidal et al. 2017, 2019; Biscoveanu et al. 2020). Including these features can enhance the precision of multi-population inference, help fighting correlations, and improve the understanding of each formation channel. We leave this extension of multi-dimensional BBH parameters in the 3G era as a future work.

## ACKNOWLEDGMENTS

The authors would like to thank Emanuele Berti, Hsin-Yu Chen, Carl Haster, and the LVK’s rate and population working group for fruitful discussions and comments. K.N. and S.V. acknowledge support of the National Science Foundation through the NSF award PHY-1836814. K.N. and S.V. are members of the LIGO Laboratory. W.M.F. is funded by the Center for Computational Astrophysics at the Flatiron Institute, which is supported by the Simons Foundation. LIGO was constructed by the California Institute of Technology and Massachusetts Institute of Technology with funding from the National Science Foundation and operates under cooperative agreement PHY-1764464. This paper carries LIGO document number LIGO-P2000540 and CE document number CEP2000007.

## APPENDIX

## A. GAUSSIAN PROCESS REGRESSION

This section provides details on the implementation of the GRP that we use to infer  $\dot{n}$  without assuming any specific functional form. We only require that  $dR/dz$  is sufficiently smooth such that  $dR/dz$  can be described by a piecewise-constant function over  $W = 30$  redshift bins, which are uniformly distributed in linear space in the range  $0 \leq z \leq 15$ . The merger rate  $dR/dz$  is thus written as

$$\frac{dR}{dz} = \begin{cases} \frac{\Delta R_1}{\Delta z_1} & 0 \leq z < z_1 \\ \dots & \\ \frac{\Delta R_i}{\Delta z_i} & z_{i-1} \leq z < z_i \\ \dots & \\ \frac{\Delta R_W}{\Delta z_W} & z_{W-1} \leq z < z_W \end{cases}, \quad (\text{A1})$$

where  $\Delta R_i$  is the merger rate in  $i$ -th redshift bin  $\Delta z_i \equiv z_i - z_{i-1} = 0.5$  so that  $\sum_{i=1}^W (\Delta R_i) \equiv R$ . To make the GPR more efficient, we infer  $dR/dz$  in natural-log space. Then, we apply a squared-exponential Gaussian process prior on  $X_i \equiv \ln(\Delta R_i)$ , with a covariance kernel

$$\begin{aligned} K_{ij} &\equiv \text{Cov}(X_i, X_j) \\ &= \sigma_X^2 \exp \left[ -\frac{1}{2} \left( \frac{z_{i-1/2} - z_{j-1/2}}{l} \right)^2 \right], \end{aligned} \quad (\text{A2})$$

where  $z_{i-1/2} = \frac{1}{2}(z_i - z_{i-1})$  is the midpoint of the  $i$ -th redshift bin,  $\sigma_X^2$  is the variance of  $\{X_i\}$ , and  $l$  is the correlation length in redshift space. The multivariate Gaussian process prior on the random variable vector  $\mathbf{X} \equiv \{\ln(\Delta R_i)\}$  with a mean vector  $\boldsymbol{\mu}_X$  and a covariance matrix  $\mathbf{K} \equiv \{K_{ij}\}$  is then,

$$\mathcal{G}(\mathbf{X} | \boldsymbol{\mu}_X, \sigma_X, l) \equiv \mathcal{N}[\mathbf{X} | \boldsymbol{\mu}_X, \mathbf{K}(\sigma_X, l)]. \quad (\text{A3})$$

The kernel  $\mathbf{K}$  enforces the smoothness of  $dR/dz$  on scales that are comparable to or larger than  $l$ , which may be much larger than the bin spacing if the data support it, and prevents from over-fitting when  $W$  is large (Foreman-Mackey et al. 2014). To further enhance the sampling efficiency, we utilize the Cholesky factorization to decompose  $\mathbf{K}$  into a

lower-triangular matrix  $\mathbf{L}$  such that

$$\mathbf{X} \equiv \mu_X + \mathbf{L}(\sigma_X, l)\boldsymbol{\eta} \quad (\text{A4})$$

follows the same Gaussian process prior  $\mathcal{G}$  by drawing  $\boldsymbol{\eta}$  from a multivariate standard normal distribution. A common choice of  $\mu_X$  is a constant mean vector  $\mu_X \mathbf{1}$ . Since we know that  $dR/dz$  has a strong dependence of the redshifted differential comoving volume  $dV_c/dz/(1+z)$ , we further impose the mean of the Gaussian process prior to be the natural log of  $dV_c/dz/(1+z)$  (normalized to  $N_{\text{obs}}$  within the comoving volume  $V_c$  and the observation time  $T$ ) with a common shift  $\Delta\mu_X$ , i.e.

$$\{\mu_{X,i}\} = \left\{ \ln \left( \frac{N_{\text{obs}}}{V_c T} \int_{z_{i-1}}^{z_i} \frac{1}{1+z} \frac{dV_c}{dz} dz \right) + \Delta\mu_X \right\}, \quad (\text{A5})$$

and we treat  $\Delta\mu_X$ , which is a single variable, as an additional parameter to include any possible fluctuation in the normalization  $R$ . We then obtain  $\dot{n}$  from  $dR/dz$  divided by the differential volume in each bin. Altogether, the  $W+3=33$  hyper-parameters in the Gaussian process regression are thus

$$\boldsymbol{\Lambda}_{\text{GPR}} = (\{\eta_i\}_{i=1}^W, \Delta\mu_X, \sigma_X, l). \quad (\text{A6})$$

## B. PHENOMENOLOGICAL MODEL

Directly modeling the volumetric merger rate  $\dot{n}$  of a subpopulation as a function of astrophysical quantities, such as various distributions of initial stellar mass, mass/radius of star clusters, BH natal kicks, or stellar metallicity, requires detailed stellar evolution or N-body simulations which are computationally expensive. To facilitate our analysis, we model the three formation channels phenomenologically. For field, we follow the Madau-Dickinson functional form <sup>4</sup>:

$$\dot{n}_{\text{F}}(z | \alpha_{\text{F}}, \beta_{\text{F}}, C_{\text{F}}) \propto \frac{(1+z)^{\alpha_{\text{F}}}}{1 + \left(\frac{1+z}{C_{\text{F}}}\right)^{\beta_{\text{F}}}}, \quad (\text{B7})$$

where  $\alpha_{\text{F}}$ ,  $\beta_{\text{F}}$  and  $C_{\text{F}}$  are unknown parameters that characterize the upward slope at  $z \lesssim C_{\text{F}} - 1$ , the downward slope at  $z \gtrsim C_{\text{F}} - 1$ , and the peak location of the volumetric merger rate density, respectively.

For cluster binaries, we describe the volumetric merger rate as a log-normal distribution in cosmic time, which we treat as a function of redshift:

$$\dot{n}_{\text{G}}(z | \mu_{\text{G}}, \sigma_{\text{G}}, t_{\text{G}}) \propto \text{LogNorm}(t(z) - t_{\text{G}} | \mu_{\text{G}}, \sigma_{\text{G}}), \quad (\text{B8})$$

where  $t(z)$  is the cosmic time as a function of redshift, and  $\text{LogNorm}$  is the standard lognormal distribution of the argument  $t - t_{\text{G}}$  parameterized by  $\mu_{\text{G}}$  and  $\sigma_{\text{G}}$ . The additional parameter,  $t_{\text{G}}$ , is a reference time that mark the birth of the first cluster binaries.

For Pop III, we use the following functional form:

$$\dot{n}_{\text{III}}(z | a_{\text{III}}, b_{\text{III}}, z_{\text{III}}) \propto \frac{e^{a_{\text{III}}(z-z_{\text{III}})}}{a_{\text{III}} + b_{\text{III}}e^{(a_{\text{III}}+b_{\text{III}})(z-z_{\text{III}})}}, \quad (\text{B9})$$

where  $a_{\text{III}}$ ,  $b_{\text{III}}$  and  $z_{\text{III}}$  characterize the upward slope at  $z < z_{\text{III}}$ , the downward slope at  $z > z_{\text{III}}$ , and the peak location of the volumetric merger rate density, respectively.

We have verified that these three phenomenological models can fit well the data from population synthesis analysis (Belczynski et al. 2016; Rodriguez & Loeb 2018; Belczynski et al. 2017) for values of their arguments given in Eqs. (B7), (B8) and (B9).

We define the branching ratio between field and cluster binaries,  $\tilde{f}_{\text{G}}$  implicitly through the equations:

<sup>4</sup> Note that while we use the same *form* for the equation, we do *not* assume that the numerical coefficients are the same of the standard Madau-Dickinson SFR

$$f_G \equiv \tilde{f}_G (1 - f_{\text{III}}), \quad (\text{B10})$$

$$f_F \equiv \left(1 - \tilde{f}_G\right) (1 - f_{\text{III}}), \quad (\text{B11})$$

where  $\{f_k\}$  are the original fractions of Eq. (6).

Therefore, there are a total of 12 hyper-parameters in the phenomenological model:

$$\Lambda_{\text{PM}} = \left(\alpha_F, \beta_F, C_F, \mu_G, \sigma_G, t_G, a_{\text{III}}, b_{\text{III}}, z_{\text{III}}, \tilde{f}_G, f_{\text{III}}, R^d\right). \quad (\text{B12})$$

### C. HYPER-PRIORS

The priors of all of the  $\Lambda_{\text{GPR}}$  hyper-parameters are tabulated in Table. 1.

**Table 1.** Hyper-priors for the GPR model.

$\Lambda_{\text{GPR},i}$	Prior function	Prior parameters	Domain
$\eta_i$	Normal	$(\mu_N, \sigma_N) = (0, 1)$	$(-\infty, +\infty)$
$\Delta\mu_X$	Normal	$(\mu_N, \sigma_N) = (0, 10)$	$(-\infty, +\infty)$
$\sigma_X$	Lognormal	$(\mu_{\text{LN}}, \sigma_{\text{LN}}) = (0, 4)$	$(0, +\infty)$
$l$	Lognormal	$(\mu_{\text{LN}}, \sigma_{\text{LN}}) = (0, \frac{1}{2} \ln(10))$	$(0, +\infty)$

The priors of all the  $\Lambda_{\text{PM}}$  hyper-parameters are tabulated in Table. 2. The choice of lognormal priors is made to

**Table 2.** Hyper-priors for the phenomenological models.

$\Lambda_{\text{PM},i}$	Prior function	Prior parameters	Domain
$\alpha_F$	Lognormal	$(\mu_{\text{LN}}, \sigma_{\text{LN}}) = (\hat{\alpha}_F, 0.25)^{\text{a}}$	$(0, 10]$
$\beta_F$	Lognormal	$(\mu_{\text{LN}}, \sigma_{\text{LN}}) = (\hat{\beta}_F, 0.25)$	$(0, 20]$
$C_F$	Lognormal	$(\mu_{\text{LN}}, \sigma_{\text{LN}}) = (\hat{C}_F, 0.25)$	$(0, 6]$
$\mu_G$	Lognormal	$(\mu_{\text{LN}}, \sigma_{\text{LN}}) = (\hat{\mu}_G, 0.25)$	$(0, 5]$
$\sigma_G$	Lognormal	$(\mu_{\text{LN}}, \sigma_{\text{LN}}) = (\hat{\sigma}_G, 0.25)$	$(0, 5]$
$t_G$	Lognormal	$(\mu_{\text{LN}}, \sigma_{\text{LN}}) = (\hat{t}_G, 0.25)$	$(0, 2.0]$
$a_{\text{III}}$	Lognormal	$(\mu_{\text{LN}}, \sigma_{\text{LN}}) = (\hat{a}_{\text{III}}, 0.5)$	$(0, 2]$
$b_{\text{III}}$	Lognormal	$(\mu_{\text{LN}}, \sigma_{\text{LN}}) = (\hat{b}_{\text{III}}, 1)$	$(0, 2]$
$z_{\text{III}}$	Normal	$(\mu_N, \sigma_N) = (\hat{z}_{\text{III}}, 2)^{\text{b}}$	$[8, 20]$
$f_{\text{III}}$	Uniform	—	$[0, 0.5]$
$\tilde{f}_G$	Uniform	—	$[0, 1.0]$
$R^d$	Half Cauchy	$\gamma_C = N_{\text{obs}}^{\text{c}}$	$[0, +\infty]$

<sup>a</sup>  $\mu_{\text{LN}}$  and  $\sigma_{\text{LN}}$  are the mean and standard deviation of the lognormal distribution, respectively.

<sup>b</sup>  $\mu_N$  and  $\sigma_N$  are the mean and standard deviation of the normal distribution, respectively.

<sup>c</sup>  $\gamma_C$  is the scale parameter of the Cauchy distribution.

restrict each model always carrying a characteristic peak within the redshift range, rather than increasing or decreasing monotonically. The gaussian prior and the domain of  $z_{\text{III}}$  ensure that the peak of  $\dot{n}_{\text{III}}$  lies at high redshift  $z \geq 8$  and prevents  $\dot{n}_{\text{III}}$  from mimicking the two dominating channels which have peaks at low redshift  $z \lesssim 3$ .

## REFERENCES

Aasi, J., et al. 2015, *Class. Quant. Grav.*, 32, 074001,  
doi: [10.1088/0264-9381/32/7/074001](https://doi.org/10.1088/0264-9381/32/7/074001)

Abbott, B., et al. 2019a, *Phys. Rev. X*, 9, 031040,  
doi: [10.1103/PhysRevX.9.031040](https://doi.org/10.1103/PhysRevX.9.031040)

- . 2019b, *Astrophys. J. Lett.*, 882, L24, doi: [10.3847/2041-8213/ab3800](https://doi.org/10.3847/2041-8213/ab3800)
- Abbott, B. P., et al. 2016, *Phys. Rev. D*, 93, 112004, doi: [10.1103/PhysRevD.93.112004](https://doi.org/10.1103/PhysRevD.93.112004)
- . 2017, *Class. Quant. Grav.*, 34, 044001, doi: [10.1088/1361-6382/aa51f4](https://doi.org/10.1088/1361-6382/aa51f4)
- Abbott, R., et al. 2020a, arXiv e-print. <https://arxiv.org/abs/2010.14527>
- . 2020b, arXiv e-print. <https://arxiv.org/abs/2010.14533>
- . 2020c, *Phys. Rev. Lett.*, 125, 101102, doi: [10.1103/PhysRevLett.125.101102](https://doi.org/10.1103/PhysRevLett.125.101102)
- . 2020d, *Astrophys. J. Lett.*, 900, L13, doi: [10.3847/2041-8213/aba493](https://doi.org/10.3847/2041-8213/aba493)
- Acernese, F., et al. 2015, *Class. Quant. Grav.*, 32, 024001, doi: [10.1088/0264-9381/32/2/024001](https://doi.org/10.1088/0264-9381/32/2/024001)
- Ade, P., et al. 2016, *Astron. Astrophys.*, 594, A13, doi: [10.1051/0004-6361/201525830](https://doi.org/10.1051/0004-6361/201525830)
- Adhikari, R. X., et al. 2019, *Class. Quant. Grav.*, 36, 245010, doi: [10.1088/1361-6382/ab3eff](https://doi.org/10.1088/1361-6382/ab3eff)
- Ali-Haïmoud, Y., Kovetz, E. D., & Kamionkowski, M. 2017, *Phys. Rev. D*, 96, 123523, doi: [10.1103/PhysRevD.96.123523](https://doi.org/10.1103/PhysRevD.96.123523)
- Amaro-Seoane, P., et al. 2017, ArXiv e-print. <https://arxiv.org/abs/1702.00786>
- Antonini, F., & Gieles, M. 2020, arXiv e-print. <https://arxiv.org/abs/2009.01861>
- Arvanitaki, A., Baryakhtar, M., Dimopoulos, S., Dubovsky, S., & Lasenby, R. 2017, *Phys. Rev.*, D95, 043001, doi: [10.1103/PhysRevD.95.043001](https://doi.org/10.1103/PhysRevD.95.043001)
- Aso, Y., Michimura, Y., Somiya, K., et al. 2013, *Phys. Rev. D*, 88, 043007, doi: [10.1103/PhysRevD.88.043007](https://doi.org/10.1103/PhysRevD.88.043007)
- Baraffe, I., Heger, A., & Woosley, S. 2001, *Astrophys. J.*, 550, 890, doi: [10.1086/319808](https://doi.org/10.1086/319808)
- Bartos, I., Kocsis, B., Haiman, Z., & Márka, S. 2017, *Astrophys. J.*, 835, 165, doi: [10.3847/1538-4357/835/2/165](https://doi.org/10.3847/1538-4357/835/2/165)
- Bavera, S. S., et al. 2020a, ArXiv e-print. <https://arxiv.org/abs/2010.16333>
- Bavera, S. S., Fragos, T., Qin, Y., et al. 2020b, *Astron. Astrophys.*, 635, A97, doi: [10.1051/0004-6361/201936204](https://doi.org/10.1051/0004-6361/201936204)
- Belczynski, K., Holz, D. E., Bulik, T., & O’Shaughnessy, R. 2016, *Nature*, 534, 512, doi: [10.1038/nature18322](https://doi.org/10.1038/nature18322)
- Belczynski, K., Ryu, T., Perna, R., et al. 2017, *Mon. Not. Roy. Astron. Soc.*, 471, 4702, doi: [10.1093/mnras/stx1759](https://doi.org/10.1093/mnras/stx1759)
- Belczynski, K., et al. 2020, *Astron. Astrophys.*, 636, A104, doi: [10.1051/0004-6361/201936528](https://doi.org/10.1051/0004-6361/201936528)
- Bird, S., Cholis, I., Muñoz, J. B., et al. 2016, *Phys. Rev. Lett.*, 116, 201301, doi: [10.1103/PhysRevLett.116.201301](https://doi.org/10.1103/PhysRevLett.116.201301)
- Biscoveanu, S., Isi, M., Vitale, S., & Varma, V. 2020, ArXiv e-print. <https://arxiv.org/abs/2007.09156>
- Boehm, C., Kobakhidze, A., O’Hare, C. A., Picker, Z. S., & Sakellariadou, M. 2020, ArXiv e-print. <https://arxiv.org/abs/2008.10743>
- Bouffanaïs, Y., Mapelli, M., Gerosa, D., et al. 2019, *Astrophys. J.*, 886, doi: [10.3847/1538-4357/ab4a79](https://doi.org/10.3847/1538-4357/ab4a79)
- Breivik, K., et al. 2020, *Astrophys. J.*, 898, 71, doi: [10.3847/1538-4357/ab9d85](https://doi.org/10.3847/1538-4357/ab9d85)
- Brito, R., Ghosh, S., Barausse, E., et al. 2017, *Phys. Rev.*, D96, 064050, doi: [10.1103/PhysRevD.96.064050](https://doi.org/10.1103/PhysRevD.96.064050)
- Broekgaarden, F. S., Justham, S., de Mink, S. E., et al. 2019, *Mon. Not. Roy. Astron. Soc.*, 490, 5228, doi: [10.1093/mnras/stz2558](https://doi.org/10.1093/mnras/stz2558)
- Callister, T., Farr, W., & Renzo, M. 2020a, arXiv e-print. <https://arxiv.org/abs/2011.09570>
- Callister, T., Fishbach, M., Holz, D., & Farr, W. 2020b, *Astrophys. J. Lett.*, 896, L32, doi: [10.3847/2041-8213/ab9743](https://doi.org/10.3847/2041-8213/ab9743)
- Carr, B. J., & Hawking, S. 1974, *Mon. Not. Roy. Astron. Soc.*, 168, 399
- Chruslinska, M., Nelemans, G., & Belczynski, K. 2019, *Mon. Not. Roy. Astron. Soc.*, 482, 5012, doi: [10.1093/mnras/sty3087](https://doi.org/10.1093/mnras/sty3087)
- Clesse, S., & García-Bellido, J. 2017, *Phys. Dark Univ.*, 15, 142, doi: [10.1016/j.dark.2016.10.002](https://doi.org/10.1016/j.dark.2016.10.002)
- de Mink, S., & Belczynski, K. 2015, *Astrophys. J.*, 814, 58, doi: [10.1088/0004-637X/814/1/58](https://doi.org/10.1088/0004-637X/814/1/58)
- de Souza, R. S., Yoshida, N., & Ioka, K. 2011, *Astron. Astrophys.*, 533, A32, doi: [10.1051/0004-6361/201117242](https://doi.org/10.1051/0004-6361/201117242)
- Di Carlo, U. N., Giacobbo, N., Mapelli, M., et al. 2019, *Mon. Not. Roy. Astron. Soc.*, 487, 2947, doi: [10.1093/mnras/stz1453](https://doi.org/10.1093/mnras/stz1453)
- Doctor, Z., Wysocki, D., O’Shaughnessy, R., Holz, D. E., & Farr, B. 2019, ArXiv e-print, doi: [10.3847/1538-4357/ab7fac](https://doi.org/10.3847/1538-4357/ab7fac)
- Dominik, M., Belczynski, K., Fryer, C., et al. 2012, *Astrophys. J.*, 759, 52, doi: [10.1088/0004-637X/759/1/52](https://doi.org/10.1088/0004-637X/759/1/52)
- . 2013, *Astrophys. J.*, 779, 72, doi: [10.1088/0004-637X/779/1/72](https://doi.org/10.1088/0004-637X/779/1/72)
- Dominik, M., Berti, E., O’Shaughnessy, R., et al. 2015, *Astrophys. J.*, 806, 263, doi: [10.1088/0004-637X/806/2/263](https://doi.org/10.1088/0004-637X/806/2/263)
- El-Badry, K., Quataert, E., Weisz, D. R., Choksi, N., & Boylan-Kolchin, M. 2019, *MNRAS*, 482, 4528, doi: [10.1093/mnras/sty3007](https://doi.org/10.1093/mnras/sty3007)
- Farmer, R., Renzo, M., de Mink, S., Fishbach, M., & Justham, S. 2020, *Astrophys. J. Lett.*, 902, L36, doi: [10.3847/2041-8213/abbadd](https://doi.org/10.3847/2041-8213/abbadd)
- Farr, B., Holz, D. E., & Farr, W. M. 2018, *Astrophys. J. Lett.*, 854, L9, doi: [10.3847/2041-8213/aaaa64](https://doi.org/10.3847/2041-8213/aaaa64)

- Farr, W. M., Gair, J. R., Mandel, I., & Cutler, C. 2015, *Phys. Rev. D*, 91, 023005, doi: [10.1103/PhysRevD.91.023005](https://doi.org/10.1103/PhysRevD.91.023005)
- Farr, W. M., Stevenson, S., Coleman Miller, M., et al. 2017, *Nature*, 548, 426, doi: [10.1038/nature23453](https://doi.org/10.1038/nature23453)
- Fishbach, M., Farr, W. M., & Holz, D. E. 2020, *Astrophys. J. Lett.*, 891, L31, doi: [10.3847/2041-8213/ab77c9](https://doi.org/10.3847/2041-8213/ab77c9)
- Fishbach, M., & Holz, D. E. 2017, *Astrophys. J. Lett.*, 851, L25, doi: [10.3847/2041-8213/aa9bf6](https://doi.org/10.3847/2041-8213/aa9bf6)
- . 2020, ArXiv e-print, doi: [10.3847/2041-8213/abc827](https://doi.org/10.3847/2041-8213/abc827)
- Fishbach, M., Holz, D. E., & Farr, B. 2017, *Astrophys. J. Lett.*, 840, L24, doi: [10.3847/2041-8213/aa7045](https://doi.org/10.3847/2041-8213/aa7045)
- Fishbach, M., Holz, D. E., & Farr, W. M. 2018, *Astrophys. J. Lett.*, 863, L41, doi: [10.3847/2041-8213/aad800](https://doi.org/10.3847/2041-8213/aad800)
- Foreman-Mackey, D., Hogg, D. W., & Morton, T. D. 2014, *ApJ*, 795, 64, doi: [10.1088/0004-637X/795/1/64](https://doi.org/10.1088/0004-637X/795/1/64)
- Fragione, G., & Loeb, A. 2020, ArXiv e-print. <https://arxiv.org/abs/2011.08935>
- Gaskin, J. A., et al. 2019, *Journal of Astronomical Telescopes, Instruments, and Systems*, 5, 1, doi: [10.1117/1.JATIS.5.2.021001](https://doi.org/10.1117/1.JATIS.5.2.021001)
- Gerosa, D., & Berti, E. 2017, *Phys. Rev. D*, 95, 124046, doi: [10.1103/PhysRevD.95.124046](https://doi.org/10.1103/PhysRevD.95.124046)
- Gerosa, D., Vitale, S., & Berti, E. 2020, *Phys. Rev. Lett.*, 125, 101103, doi: [10.1103/PhysRevLett.125.101103](https://doi.org/10.1103/PhysRevLett.125.101103)
- Greene, J. E., Strader, J., & Ho, L. C. 2020, *Annual Reviews of Astronomy & Astrophysics*, 58, 257, doi: [10.1146/annurev-astro-032620-021835](https://doi.org/10.1146/annurev-astro-032620-021835)
- Gröbner, M., Ishibashi, W., Tiwari, S., Haney, M., & Jetzer, P. 2020, *Astron. Astrophys.*, 638, A119, doi: [10.1051/0004-6361/202037681](https://doi.org/10.1051/0004-6361/202037681)
- Hall, A., Gow, A. D., & Byrnes, C. T. 2020, ArXiv e-print. <https://arxiv.org/abs/2008.13704>
- Hall, E. D., & Evans, M. 2019, *Class. Quant. Grav.*, 36, 225002, doi: [10.1088/1361-6382/ab41d6](https://doi.org/10.1088/1361-6382/ab41d6)
- Hartwig, T., Volonteri, M., Bromm, V., et al. 2016, *Mon. Not. Roy. Astron. Soc.*, 460, L74, doi: [10.1093/mnrasl/slw074](https://doi.org/10.1093/mnrasl/slw074)
- Hütsi, G., Raidal, M., Vaskonen, V., & Veermäe, H. 2020. <https://arxiv.org/abs/2012.02786>
- Kimball, C., Berry, C. P., & Kalogera, V. 2019, ArXiv e-print, doi: [10.3847/2515-5172/ab66be](https://doi.org/10.3847/2515-5172/ab66be)
- Kimball, C., Talbot, C., L. Berry, C. P., et al. 2020a, *Astrophys. J.*, 900, 177, doi: [10.3847/1538-4357/aba518](https://doi.org/10.3847/1538-4357/aba518)
- Kimball, C., et al. 2020b, arXiv e-print. <https://arxiv.org/abs/2011.05332>
- Kinugawa, T., Inayoshi, K., Hotokezaka, K., Nakauchi, D., & Nakamura, T. 2014, *Mon. Not. Roy. Astron. Soc.*, 442, 2963, doi: [10.1093/mnras/stu1022](https://doi.org/10.1093/mnras/stu1022)
- Kinugawa, T., Miyamoto, A., Kanda, N., & Nakamura, T. 2016, *Mon. Not. Roy. Astron. Soc.*, 456, 1093, doi: [10.1093/mnras/stv2624](https://doi.org/10.1093/mnras/stv2624)
- Kinugawa, T., Nakamura, T., & Nakano, H. 2020, arXiv e-print. <https://arxiv.org/abs/2009.06922>
- Kremer, K., Spera, M., Becker, D., et al. 2020, *Astrophys. J.*, 903, 45, doi: [10.3847/1538-4357/abb945](https://doi.org/10.3847/1538-4357/abb945)
- Lower, M. E., Thrane, E., Lasky, P. D., & Smith, R. 2018, *Phys. Rev. D*, 98, 083028, doi: [10.1103/PhysRevD.98.083028](https://doi.org/10.1103/PhysRevD.98.083028)
- Madau, P., & Dickinson, M. 2014, *Ann. Rev. Astron. Astrophys.*, 52, 415, doi: [10.1146/annurev-astro-081811-125615](https://doi.org/10.1146/annurev-astro-081811-125615)
- Maggiore, M., et al. 2020, *JCAP*, 03, 050, doi: [10.1088/1475-7516/2020/03/050](https://doi.org/10.1088/1475-7516/2020/03/050)
- Mandel, I., Farr, W. M., Colonna, A., et al. 2017, *Mon. Not. Roy. Astron. Soc.*, 465, 3254, doi: [10.1093/mnras/stw2883](https://doi.org/10.1093/mnras/stw2883)
- Mandel, I., Farr, W. M., & Gair, J. R. 2019, *Mon. Not. Roy. Astron. Soc.*, 486, 1086, doi: [10.1093/mnras/stz896](https://doi.org/10.1093/mnras/stz896)
- Mapelli, M., Giacobbo, N., Santoliquido, F., & Artale, M. C. 2019, *Mon. Not. Roy. Astron. Soc.*, 487, 2, doi: [10.1093/mnras/stz1150](https://doi.org/10.1093/mnras/stz1150)
- McCuller, L., et al. 2020, *Phys. Rev. Lett.*, 124, 171102, doi: [10.1103/PhysRevLett.124.171102](https://doi.org/10.1103/PhysRevLett.124.171102)
- Miller, S., Callister, T. A., & Farr, W. 2020, *Astrophys. J.*, 895, 128, doi: [10.3847/1538-4357/ab80c0](https://doi.org/10.3847/1538-4357/ab80c0)
- Morscher, M., Pattabiraman, B., Rodriguez, C., Rasio, F. A., & Umbreit, S. 2015, *ApJ*, 800, 9, doi: [10.1088/0004-637X/800/1/9](https://doi.org/10.1088/0004-637X/800/1/9)
- Ng, K. K., Hannuksela, O. A., Vitale, S., & Li, T. G. 2019, arXiv e-print. <https://arxiv.org/abs/1908.02312>
- Ng, K. K., Vitale, S., Hannuksela, O. A., & Li, T. G. 2020, arXiv e-print. <https://arxiv.org/abs/2011.06010>
- O’Shaughnessy, R., Bellovary, J., Brooks, A., et al. 2017, *Mon. Not. Roy. Astron. Soc.*, 464, 2831, doi: [10.1093/mnras/stw2550](https://doi.org/10.1093/mnras/stw2550)
- Portegies Zwart, S. F., & McMillan, S. L. W. 2000, *ApJ*, 528, L17, doi: [10.1086/312422](https://doi.org/10.1086/312422)
- Punturo, M., et al. 2010, *Class. Quant. Grav.*, 27, 194002, doi: [10.1088/0264-9381/27/19/194002](https://doi.org/10.1088/0264-9381/27/19/194002)
- Raidal, M., Spethmann, C., Vaskonen, V., & Veermäe, H. 2019, *JCAP*, 02, 018, doi: [10.1088/1475-7516/2019/02/018](https://doi.org/10.1088/1475-7516/2019/02/018)
- Raidal, M., Vaskonen, V., & Veermäe, H. 2017, *JCAP*, 09, 037, doi: [10.1088/1475-7516/2017/09/037](https://doi.org/10.1088/1475-7516/2017/09/037)
- Regimbau, T., Evans, M., Christensen, N., et al. 2017, *Phys. Rev. Lett.*, 118, 151105, doi: [10.1103/PhysRevLett.118.151105](https://doi.org/10.1103/PhysRevLett.118.151105)
- Reitze, D., et al. 2019, *Bull. Am. Astron. Soc.*, 51, 035. <https://arxiv.org/abs/1907.04833>

- Rodriguez, C. L., Chatterjee, S., & Rasio, F. A. 2016, *Phys. Rev. D*, 93, 084029, doi: [10.1103/PhysRevD.93.084029](https://doi.org/10.1103/PhysRevD.93.084029)
- Rodriguez, C. L., & Loeb, A. 2018, *Astrophys. J. Lett.*, 866, L5, doi: [10.3847/2041-8213/aae377](https://doi.org/10.3847/2041-8213/aae377)
- Rodriguez, C. L., Morscher, M., Pattabiraman, B., et al. 2015, *Phys. Rev. Lett.*, 115, 051101, doi: [10.1103/PhysRevLett.115.051101](https://doi.org/10.1103/PhysRevLett.115.051101)
- Romero-Shaw, I. M., Kremer, K., Lasky, P. D., Thrane, E., & Samsing, J. 2020, arXiv e-print. <https://arxiv.org/abs/2011.14541>
- Roulet, J., Venumadhav, T., Zackay, B., Dai, L., & Zaldarriaga, M. 2020, arXiv e-print. <https://arxiv.org/abs/2008.07014>
- Safarzadeh, M., Berger, E., Ng, K. K.-Y., et al. 2019, *Astrophys. J. Lett.*, 878, L13, doi: [10.3847/2041-8213/ab22be](https://doi.org/10.3847/2041-8213/ab22be)
- Safarzadeh, M., Farr, W. M., & Ramirez-Ruiz, E. 2020, *Astrophys. J.*, 894, 129, doi: [10.3847/1538-4357/ab80be](https://doi.org/10.3847/1538-4357/ab80be)
- Samsing, J., Bartos, I., D’Orazio, D., et al. 2020, ArXiv e-print. <https://arxiv.org/abs/2010.09765>
- Santoliquido, F., Mapelli, M., Giacobbo, N., Bouffanais, Y., & Artale, M. C. 2020, arXiv e-print. <https://arxiv.org/abs/2009.03911>
- Sasaki, M., Suyama, T., Tanaka, T., & Yokoyama, S. 2016, *Phys. Rev. Lett.*, 117, 061101, doi: [10.1103/PhysRevLett.117.061101](https://doi.org/10.1103/PhysRevLett.117.061101)
- Stevenson, S., Ohme, F., & Fairhurst, S. 2015, *Astrophys. J.*, 810, 58, doi: [10.1088/0004-637X/810/1/58](https://doi.org/10.1088/0004-637X/810/1/58)
- Stevenson, S., Vigna-Gómez, A., Mandel, I., et al. 2017, *Nature Commun.*, 8, 14906, doi: [10.1038/ncomms14906](https://doi.org/10.1038/ncomms14906)
- Tagawa, H., Haiman, Z., Bartos, I., & Kocsis, B. 2020a, *Astrophys. J.*, 899, 26, doi: [10.3847/1538-4357/aba2cc](https://doi.org/10.3847/1538-4357/aba2cc)
- Tagawa, H., Haiman, Z., & Kocsis, B. 2020b, *Astrophys. J.*, 898, 25, doi: [10.3847/1538-4357/ab9b8c](https://doi.org/10.3847/1538-4357/ab9b8c)
- Tagawa, H., Kocsis, B., Haiman, Z., et al. 2020c, arXiv e-print. <https://arxiv.org/abs/2012.00011>
- Talbot, C., & Thrane, E. 2017, *Phys. Rev. D*, 96, 023012, doi: [10.1103/PhysRevD.96.023012](https://doi.org/10.1103/PhysRevD.96.023012)
- . 2018, *Astrophys. J.*, 856, 173, doi: [10.3847/1538-4357/aab34c](https://doi.org/10.3847/1538-4357/aab34c)
- Tanikawa, A., Kinugawa, T., Yoshida, T., Hijikawa, K., & Umeda, H. 2020, arXiv e-print. <https://arxiv.org/abs/2010.07616>
- Thrane, E., & Talbot, C. 2019, *Publ. Astron. Soc. Austral.*, 36, e010, doi: [10.1017/pasa.2019.2](https://doi.org/10.1017/pasa.2019.2)
- Tiwari, V., & Fairhurst, S. 2020, ArXiv e-print. <https://arxiv.org/abs/2011.04502>
- Van Den Broeck, C. 2010, in *On recent developments in theoretical and experimental general relativity, astrophysics and relativistic field theories. Proceedings, 12th Marcel Grossmann Meeting on General Relativity, Paris, France, July 12-18, 2009. Vol. 1-3, 1682–1685*, doi: [10.1142/9789814374552\\_0302](https://doi.org/10.1142/9789814374552_0302)
- Van Den Broeck, C. 2014, *J. Phys. Conf. Ser.*, 484, 012008, doi: [10.1088/1742-6596/484/1/012008](https://doi.org/10.1088/1742-6596/484/1/012008)
- Vangioni, E., Olive, K., Prestegard, T., et al. 2015, *Mon. Not. Roy. Astron. Soc.*, 447, 2575, doi: [10.1093/mnras/stu2600](https://doi.org/10.1093/mnras/stu2600)
- Venumadhav, T., Zackay, B., Roulet, J., Dai, L., & Zaldarriaga, M. 2020, *Phys. Rev. D*, 101, 083030, doi: [10.1103/PhysRevD.101.083030](https://doi.org/10.1103/PhysRevD.101.083030)
- Vitale, S. 2016, *Phys. Rev. D*, 94, 121501, doi: [10.1103/PhysRevD.94.121501](https://doi.org/10.1103/PhysRevD.94.121501)
- . 2020, arXiv e-print. <https://arxiv.org/abs/2007.05579>
- Vitale, S., & Evans, M. 2017, *Phys. Rev. D*, 95, 064052, doi: [10.1103/PhysRevD.95.064052](https://doi.org/10.1103/PhysRevD.95.064052)
- Vitale, S., Farr, W. M., Ng, K., & Rodriguez, C. L. 2019, *Astrophys. J. Lett.*, 886, L1, doi: [10.3847/2041-8213/ab50c0](https://doi.org/10.3847/2041-8213/ab50c0)
- Vitale, S., Lynch, R., Sturani, R., & Graff, P. 2017, *Class. Quant. Grav.*, 34, 03LT01, doi: [10.1088/1361-6382/aa552e](https://doi.org/10.1088/1361-6382/aa552e)
- Vitale, S., & Whittle, C. 2018, *Phys. Rev. D*, 98, 024029, doi: [10.1103/PhysRevD.98.024029](https://doi.org/10.1103/PhysRevD.98.024029)
- Wong, K., Franciolini, G., De Luca, V., et al. 2020a, ArXiv e-print. <https://arxiv.org/abs/2011.01865>
- Wong, K. W., Breivik, K., Kremer, K., & Callister, T. 2020b, arXiv e-print. <https://arxiv.org/abs/2011.03564>
- Wysocki, D., Lange, J., & O’Shaughnessy, R. 2019, *Phys. Rev. D*, 100, 043012, doi: [10.1103/PhysRevD.100.043012](https://doi.org/10.1103/PhysRevD.100.043012)
- Yang, Y., Bartos, I., Haiman, Z., et al. 2020, *Astrophys. J.*, 896, 138, doi: [10.3847/1538-4357/ab91b4](https://doi.org/10.3847/1538-4357/ab91b4)
- Yang, Y., et al. 2019, *Phys. Rev. Lett.*, 123, 181101, doi: [10.1103/PhysRevLett.123.181101](https://doi.org/10.1103/PhysRevLett.123.181101)
- Yi, S.-X., & Cheng, K. 2019, *Astrophys. J. Lett.*, 884, L12, doi: [10.3847/2041-8213/ab459a](https://doi.org/10.3847/2041-8213/ab459a)
- Yu, H., et al. 2018, *Phys. Rev. Lett.*, 120, 141102, doi: [10.1103/PhysRevLett.120.141102](https://doi.org/10.1103/PhysRevLett.120.141102)
- Zevin, M., Pankow, C., Rodriguez, C. L., et al. 2017, *Astrophys. J.*, 846, 82, doi: [10.3847/1538-4357/aa8408](https://doi.org/10.3847/1538-4357/aa8408)
- Zevin, M., Bavera, S. S., Berry, C. P., et al. 2020, arXiv e-print. <https://arxiv.org/abs/2011.10057>